Available online at www.sciencedirect.com
ScienceDirect
Continental Shelf Research 27 (2007) 832–853
CONTINENTAL SHELF RESEARCH
www.elsevier.com/locate/csr

Sediment-transport modeling on Southern Californian shelves: A ROMS case study

Meinte Blaas[e], Changming Dong[a], Patrick Marchesiello[c], James C. McWilliams[b,*], Keith D. Stolzenbach[d]

[a]*Institute of Geophysics and Planetary Physics, UCLA, Los Angeles, CA 90095-1567, USA*
[b]*Department of Atmospheric and Oceanic Sciences, UCLA, Los Angeles, CA 90095-1565, USA*
[c]*IRD, Brest, France*
[d]*Department of Civil and Environmental Engineering, UCLA, Los Angeles, CA 90095-1593, USA*
[e]*WL|Delft Hydraulics, Delft, The Netherlands*

Received 21 December 2005; received in revised form 21 July 2006; accepted 3 December 2006
Available online 20 December 2006

Abstract

Suspended sediment-transport processes in Santa Monica and San Pedro Bay are analyzed using the sediment-transport capabilities of the Regional Oceanic Modeling System (ROMS). A one-month simulation for December 2001 has been carried out with a set of nested domains. The model inputs include tides, winds, surface waves, and idealized initial sediment conditions for sand and non-cohesive silt. Apart from the control run, the sensitivity of the results to surface waves, ripple roughness and bed armoring has been analyzed. From the control experiment, the horizontal transport of sand turns out to be limited to within a few km of the nearshore erosion zones. During high wave events, silt is transported over further distances and also partly offshelf in distinct plumes. The effectiveness of horizontal silt transport depends strongly on vertical mixing due to both surface wind stress and wave-enhanced bottom stress. High wave events coincident with strong winds (hence strong vertical mixing) are the most optimal conditions for sediment-transport. Excluding wave effects in the simulation shows that surface waves are the dominant factor in resuspending bed material on the Southern Californian shelves. The sensitivity experiments also show that the direct influence of additional ripple roughness on erosion and deposition is relatively weak. Switching off bed armoring locally results in increases of near-bottom concentrations by a factor of 20 for silt and a factor of 5 for sand as well as stronger spatial gradients in grain size.

Keywords: Sediment-transport; Wind waves; Shelf sea circulation; Wave boundary layer; Santa Monica Bay; San Pedro Bay

1. Introduction

In this paper, we present a numerical modeling study that aims to contribute to understanding sediment-transport processes on the shelves of Southern California. The Southern Californian waters of Santa Monica Bay and San Pedro Bay (SMB and SPB; Fig. 1) are bordered by one of the most heavily urbanized areas in the US and hence are exposed to a large variety of natural and anthropogenic sources of suspended matter (sediments and pollutants). This material can be either

*Corresponding author. Tel.: 1 310 206 2829; fax: 1 310 206 5219.
E-mail address: jcm@atmos.ucla.edu (J.C. McWilliams).

0278-4343/$ - see front matter © 2007 Elsevier Ltd. All rights reserved.
doi:10.1016/j.csr.2006.12.003

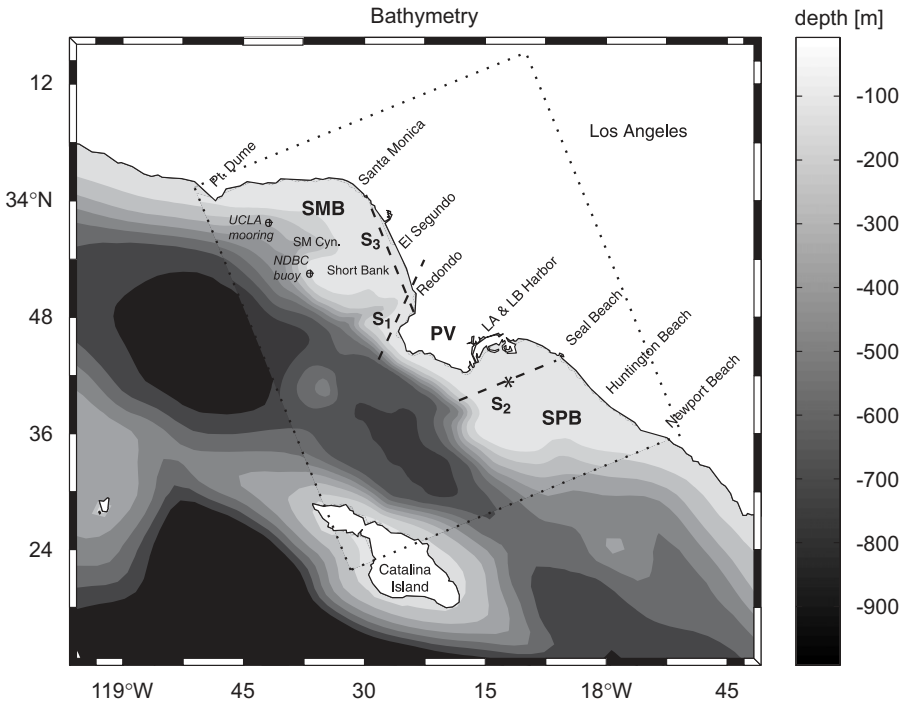

Fig. 1. Bathymetry for the innermost domain (i.e., area boxed by dotted line), with nominal resolution of 0.7 km nested within 2 km resolution grid. Dashed lines indicate the transects S_1, S_2, and S_3 (see Section 4). Geographical and buoy locations referred to in the text are indicated.

trapped in the sea-floor sediments of the bays or be resuspended and redeposited various times before ending up in the adjacent deep basins (Emery, 1960; Gorsline and Grant, 1972; Gorsline et al., 1984). An overview of recent sediment quality studies in SMB can be found in a special issue of *Marine Environmental Research*.[1]

The bed of the shelves mostly consists of sandy and silty to clayey sediments, generally fining with increasing depth (Emery, 1960; Gorsline and Grant, 1972; Sommerfield and Lee, 2003). The largest areas in both bays consist of silt and fine sand (mean grain sizes 16–125 μm). Areas are found with coarser sediments (fine to medium-grained sand, local rocky outcrops) on the mid-shelf plateaus.

Field observations suggest that on decadal time scales SMB is able to trap fine sediments coming from outside the bay (Wiberg et al., 2002; Sommerfield and Lee, 2003). Numerical modeling of sediment-transport (such as also done before by Sherwood et al., 2002 and Wiberg and Harris, 2002 for the Palos Verdes shelf, for example) may eventually improve the assessment of longer-term sediment budgets, and provide insight into the transport mechanisms.

Various hydrodynamic processes determine sediment resuspension, transport and deposition. Near-bottom orbital motions due to surface waves are generally thought to be an important factor for resuspension in the Southern Californian coastal waters. Observations by Drake et al. (1985) suggest that in SPB, for example, the tidal motion alone is generally not strong enough to suspend sediments. Video observations of wave ripples by Xu (2005) suggest that, on a 15 m deep site on the SPB shelf, the bed was active for over 70% of the time of a 20-day period in January–February 2002 with varying wave conditions. Gorsline et al. (1984) and Noble and Xu (2003) suggest that also internal waves may play a role, at least locally on the outer shelf and shelf break in SMB.

Sub-tidal currents in the bays are expected to be most effective in redistributing suspended sediments over longer distances on longer time scales. These flows are partly wind-influenced but are also strongly determined by mesoscale eddies and

[1]"On The Integrated Assessment of an Urban Water Body: Santa Monica Bay, California", edited by Lee and Weisberg (56(1–2), July–August, 2003).

filaments originating from the California Current System. Typical mesoscale eddies have dimensions similar to the embayments, and they propagate through the area on a time scale of days. Hickey (1992) and Hickey et al. (2003) give extensive discussion on the circulation in the Southern Californian Bight and adjacent Bays in relation to the California Current System. Using remote sensing data, Nezlin and DiGiacomo (2005) illustrate the importance of the mesoscale flow for plumes of riverine suspended matter in SPB.

The present paper aims to provide more insight into the physical processes that determine resuspension, transport and deposition of suspended matter on the above-mentioned shelves. To this end, a numerical model is presented, and four experiments are discussed in which we explore the relative influence of waves, currents, and vertical mixing on sediment-transport. The model experiments presented here extend earlier one-dimensional (vertical) and two-dimensional (2DV cross-shore) model studies, such as by Niedoroda et al. (1996) and Wiberg et al. (2002), and Zhang et al. (1999) and Harris and Wiberg (2001), respectively. Up to now no extensive 3D sediment-transport model study has been carried out for this area.

Presently, the ROMS sediment-transport model development is at a stage where we want to explore its qualitative behavior before embarking on more quantitative studies. Therefore, the central questions of this study are focused on process identification and reproduction of general features. Most importantly we show that the model is capable of yielding plausible results, despite some of our necessary simplifying assumptions. Second, we want to identify and quantify the role of surface waves, currents and mixing in the bays for suspended sediment-transport. Questions are: On what time and spatial scales do resuspension, transport and deposition occur? What are the source and sink areas? And how do these relate to the relative effects of surface waves, tides and mesoscale flows? What is the vertical extent of resuspension and how is that related to forcing conditions? How do results depend on parameterizations of ripples and armoring?

2. Model description

The sediment-transport model presented here is part of ROMS. ROMS is a free-surface, hydrostatic, primitive-equation model with stretched, terrain-following vertical *s*-coordinates and orthogonal, curvilinear horizontal coordinates. For a more extensive description and technical details of the hydrodynamic model as well as earlier applications to the US West Coast, we refer to Shchepetkin and McWilliams (1998, 2003, 2005), Marchesiello et al. (2001, 2003) and to Penven et al. (2006) (see also www.atmos.ucla.edu/cesr/ROMS_page.html). Warner et al. (2005) presented the sediment-transport capability in ROMS in an earlier stage and in particular focused on the dependence of sediment-transport on different turbulence closure schemes. Since that study the code has been extended with a two-layer sediment bed, taking into account the effect of mixed beds on sediment entrainment. Moreover, the combined effect of waves and currents on the bottom stress and the related parameterization of surface waves and bottom ripples have been added. The vertical eddy diffusivity scheme for the bottom layer has been adapted to incorporate the new bottom stress parameterizations. In the recent past, sediment modeling capabilities have also been developed for other hydrodynamic modeling systems, e.g., in Delft3D (Lesser et al., 2004) or COHERENS (Luyten et al., 1999), with applications primarily focused on European shelves.

2.1. Sediment concentration

Our primary motivations in the Southern Californian sediment-transport studies are water quality and flux computations on time scales of days up to seasons and on spatial scales of hundreds of meters up to tens of kilometers. The sediment fractions of particular interest are predominantly fine-grained. In this paper, we treat all sediment fractions as non-cohesive. Because of its additional complexity and lesser occurrence on the Southern California shelves, the modeling of cohesive sediments is beyond the scope of this paper. The scales of interest exceed those of individual morphologic features such as sand banks and ripples. Hence, we only take into account suspended-load transport. Bed load is considered only when it is relevant for sediment resuspension (Appendix A.1). The approach relies on the solution of the transport equation for suspended sediments, for each sediment size-class j:

$$\frac{\partial c_j}{\partial t}+\frac{\partial u_i c_j}{\partial x_i}-\frac{\partial}{\partial x_i}\left(K_i\frac{\partial c_j}{\partial x_i}\right)-w_{sj}\frac{\partial c_j}{\partial x_3}=Q_j. \quad (1)$$

Subscripts i,j denote coordinate direction (with x_3 vertically upward); c_j is the Reynolds-averaged,

wave-averaged sediment concentration of sediments in class j; u_i is velocity; K_i is the eddy diffusivity; w_{sj} is the settling velocity, dependent on sediment grain size, but independent of flow conditions and concentrations; and Q_j represents point sources or sinks (which we neglect in our cases; Section 3.6). (Repeated indices imply summation. Wherever possible without ambiguity, subscripts will be omitted in the following.)

Horizontal diffusion of sediments is not explicitly present in our applications ($K_1 = K_2 = 0\,\mathrm{m^2\,s^{-1}}$) since the advection scheme by Shchepetkin and McWilliams (1998) in ROMS is implicitly dissipative and locally adaptive to the flow and advected quantity. Vertical eddy diffusivity for tracers (K_3, further denoted as K_s) is determined using the K-profile parameterization (KPP) by Large et al. (1994). This scheme includes a bottom-boundary layer parameterization dependent on the bottom shear stress that is a wave–current combined shear stress if waves are present (Appendix A.3). In a recent process study with ROMS, Dong et al. (2006) show the robustness of the solution of mesoscale flow features with its advection and turbulence schemes.

Eq. (1) is solved separately for each size class. Independent solvers are used for the handling of vertical settling, sources and sinks, horizontal advection, vertical advection, and vertical diffusion. The vertical settling scheme includes a piece-wise parabolic method (Colella and Woodward, 1984) and a weighted, essentially non-oscillatory scheme (WENO; Liu et al., 1994). The settling scheme is not constrained by the CFL criterion, which may otherwise be violated over shallow areas. In our experiments, sea surface fluxes and point sources are absent. Lateral open boundaries are treated according to Marchesiello et al. (2001): radiation and advection conditions apply during outflow; concentrations are nudged to an external value during inflow. In our applications, open boundaries are located in deep water as much as possible such that a nudging value of zero can be used, since we expect sediment concentrations to vanish over deep water. The model does not resolve the surf zone explicitly: the computational domain is confined to the area deeper than 10 m and a no-flux condition is imposed at the coastal model boundaries.

2.2. Sediment bed and resuspension

The sediment bed is modeled as a two layer system similar to Reed et al. (1999). A relatively thin "active layer" ($h_{bed}(1) = \delta_a$) sits on top of a vertically well-mixed bulk layer or substrate ($h_{bed}(2)$). The active layer is the interface between water column and sediment bed. The thickness of the substrate varies over time. When the bed erodes, substrate sediment is mixed into the active layer. During net deposition the surplus in the active layer is mixed into the substrate. For each size class, the net flux into the water is the sum of the deposition flux ($-w_s c$) and the erosion flux E. The erosion flux E ($\mathrm{kg\,m^{-2}\,s^{-1}}$) depends on active-layer properties and the bottom stress, similar to Ariathurai and Arulanandan (1978):

$$E_j = E_{0,j}(1-p) f_j \left(\frac{\tau_b}{\tau_{cr,j}} - 1\right) \quad \text{for } \tau_b > \tau_{cr,j};$$
$$E_j = 0 \quad \text{otherwise.} \tag{2}$$

Here $E_{0,j}$ is an empirical entrainment rate; p is the sediment porosity (which in future may be made dependent on bed composition); f_j is the volumetric fraction of sediment of class j; $\tau_{cr,j}$ is the critical shear stress for class j; and τ_b is the magnitude of the shear stress on the grains (Section 2.3).

The dimensional critical (skin frictional) shear stress $\tau_{cr,j}$ beyond which sediment starts to move, is derived from the critical Shields parameter, of which the value is determined using the approximation by Soulsby and Whitehouse (1997).

The entrainment rate of a specific size class in a mixed bed may differ from that in a uniform bed. Resuspension of smaller size classes may be reduced due to hiding, and the coarser grains resuspend more easily due to exposure. Furthermore, bed erosion may become limited when selective entrainment of the fine fraction causes "bed armoring". The remaining coarser grains then inhibit resuspension of the fine grains. Several studies suggest that armoring is important on the Californian shelves (Drake and Cacchione, 1989; Wiberg et al., 1994; Reed et al., 1999). We adopt the parameterization by Garcia and Parker (1991). Although it has been derived for alluvial beds, it has been successfully applied in marine environments before by Walgreen et al. (2003). For each size class j, the modified entrainment rate becomes

$$E_{0,j} = \left(\frac{d_j}{d_{50}}\right)^{1.0} \lambda_E^5 E_{u,j}, \tag{3}$$

with $E_{u,j}$ the entrainment rate for a uniform bed of sediments of class j. λ_E is a "straining parameter" that depends on the sediment distribution in the

active layer: $\lambda_E = 1 - 0.29\sigma_\phi$ with σ_ϕ the standard deviation of the sediment distribution on the sedimentological ϕ-scale. According to Eq. (3), the erosion rate of a mixture is reduced more the less sorted the bed is. The entrainment rate of the smaller fractions is reduced compared to the coarser fractions. The armoring effect increases the more skewed the grain size distribution is towards the coarser fractions.

Because all sediment fractions are non-cohesive, the entrainment rate E_u is constant in time. Still, E_u is an empirical quantity, depending on local sediment and bed conditions. In the literature values range from about 10^{-4} to about $10^{-2}\,\mathrm{kg\,m^{-2}\,s^{-1}}$ (e.g., Smith and McLean, 1977; Drake and Cacchione, 1989; Li and Amos, 2001; Xu et al., 2002). A constant E_u is chosen for each size class, proportional to w_s and ρ_s with a proportionality constant consistent with Drake and Cacchione (1989); see Table 1.

2.3. Bottom shear stress and boundary layer

Typical conditions for sediment-transport on Southern Californian shelves are those in which strong swell and wind waves coexist with currents. Because of the interactions within the combined boundary layer, the total bed stress is greater than would be obtained from linear addition of wave and current related bottom stresses. In the past, a range of wave–current boundary layer models has been developed; e.g., by Smith (1977) and Grant and Madsen (1979). These models require the solution of a set of equations on the scale of the wave and current boundary layers. Nevertheless, to capture the enhancement of the bottom shear stress and provide an input into the parameterization for the mixing coefficients in the bottom boundary layer, application of the two-coefficient expression by Soulsby (1995) suffices. It keeps the model computationally efficient and the number of additional parameters low and in general performs as well as the more complex models. It yields the wave-averaged bed-shear stress $\bar{\tau}_{cw}$ under the combined influence of waves and currents as a function of the stresses due to waves in the absence of currents and currents in the absence of waves, respectively (see Appendix A.1).

The mobilization of sediment depends on the maximum shear stress on the grains (skin friction, using Nikuradse's roughness length). The effective bottom drag as exerted on the flow, however, includes effects of drag due to bed forms. The character of bed forms depends empirically on median grain size d_{50} in the active layer. For sandy areas ($d_{50} > 63\,\mu\mathrm{m}$) ripples may develop and total roughness is calculated according to Li and Amos (2001). The roughness due to ripples is used to determine the shear stress acting on the flow. (See Appendix A.2 for more details.)

The subgrid-scale vertical mixing within the turbulent bottom boundary layer is based on the KPP scheme. It determines the vertical profiles of the eddy diffusivity coefficients in the outer region above the unresolved wave–current boundary layer, in contrast to the computationally more demanding parameterization by Styles and Glenn (2000) for example. The KPP scheme uses the friction velocity from this inner layer as input. The bottom boundary layer parameterization is further specified in Appendix A.3.

Table 1
Sediment parameters (all experiments)

Class name	d (μm)	ρ_s (kg/m^3)	w_s (mm/s)	E_u (kg/m^2 s)	τ_{cr} (N/m^2)
Silt	24	2650	0.4	1.0×10^{-4}	0.07
Sand	125	2650	9.4	2.5×10^{-3}	0.15

The thickness of the active layer $\delta_a = 3$ mm; the initial thickness of the substrate is set to 1 m. The porosity $p = 0.4$.

3. Southern California application

3.1. Domain

The California current system drives the circulation in the area (e.g., Hickey, 1992; Hickey et al., 2003). To capture the large-scale California current system influence, an on-line nesting of four computational domains is used. The nesting is achieved by use of the Adaptive Grid Refinement In Fortran library (AGRIF, Blayo and Debreu, 1999, and http://www-lmc.imag.fr/IDOPT/AGRIF). The curvilinear grids of our US West Coast configuration have a horizontal resolution increasing from about 20 km on the outermost domain to about 0.7 km on the innermost domain with a refinement factor of 3 for each nesting step; 40 s-levels are used in the vertical. The outer domain extends from the middle of Baja California ($\approx 28^\circ$N) to the US–Canada border ($\approx 48^\circ$N). The first nested domain covers the greater Southern Californian Bight; the second nested level

covers the inner part of the Bight (Santa Barbara Channel to San Diego); and the innermost domain covers SMB and SPB and the basins directly offshore (Fig. 1).

3.2. Topography

The topography of the outer domain is interpolated from ETOPO2 (Smith and Sandwell, 1997), whereas the inner domains make use of the 0.12′ resolution bathymetry by NOAA (http://biogeo.nos.noaa.gov). Despite the use of a high-order scheme for computation of horizontal pressure gradient forces (Shchepetkin and McWilliams, 2003), a certain degree of smoothing of the bathymetry is required. This implies that the innermost domain does not fully resolve all steep smaller-scale features like the smaller canyons in the bays. However, Redondo Canyon and Santa Monica Canyon are resolved (see Fig. 1). The same bathymetry is used for the swell-wave model (Section 3.5).

3.3. Tides

Barotropic tidal currents are generally modest in the Bight (barotropic velocities of a few cm/s), but they gain strength over the shelves to up to a few tens of cm/s (Hickey, 1992). This requires the tidal currents to be represented in the model. Tidal boundary conditions are imposed at the open boundaries of the outermost domain and are derived from the OSU TOPEX/Poseidon Global Inverse Solution 6.0 (TPXO.6; Egbert and Erofeeva, 2002). Along the US West Coast the tidal signal is a mixed, predominantly semi-diurnal tide. The tides are imposed using the modified Flather and Orlanski-type conditions by Marchesiello et al. (2001).

Earlier tests on the US West Coast configuration have shown that ROMS is well capable of solving the barotropic tides. For the free surface elevation, the differences between ROMS output and TPXO.6 are no more than a few percent in the offshore. Tidal current amplitudes compare reasonably well to observed tidal currents at the mooring deployed in SMB by UCLA's Institute of the Environment (see Fig. 1). At the mooring site, ROMS reproduces the right amplitude of about 5 cm/s for the currents averaged over the top 70 m, though underestimating the u and overestimating the v-component, respectively, by about 1 cm/s leading to a slightly more circular tidal ellipse than observed. A more elaborate study of the US West Coast tides in ROMS is being done by Wang et al. (2006). Analysis of the low-pass filtered part of the model solution and UCLA mooring data of December 2001 shows that the low-frequency model currents also have the right magnitude of about 5 cm/s.

3.4. Wind and buoyancy forcing

The experiments cover the period December 1, 2001 to January 1, 2002. In general, December is a period when the low-frequency large-scale wind forcing over the eastern Pacific is relatively weak. This causes the flow in the Bight to be directed poleward, driven by the along-shore pressure gradient (see also Hickey, 1992). This poleward flow induces energetic mesoscale eddies in the SMB and SPB. December 2001 is a representative winter month in which, despite the weak large-scale wind, episodes of high local winds and waves occur that are expected to be most relevant for sediment resuspension and transport. The initial condition for the experiments reported here was the state of the solution on December 1, 2001, obtained from an 8-year simulation of the Bight (Dong et al., 2007). The thermodynamic surface forcing consists of climatological fluxes of heat, short-wave radiation, fresh-water and SST and SSS from COADS (Da Silva et al., 1994). Lateral open boundary conditions for the outermost domain are derived from climatology (Levitus et al., 1994; Levitus and Boyer, 1994). Wind forcing is obtained from a regional atmospheric modeling experiment at UCLA (Conil et al., 2007). The NCAR MM5 mesoscale model forced by NCEP ETA reanalysis data (http://www.emc.ncep.noaa.gov/) has been applied in a triple-nested set of domains (with resolutions of 54, 18, and 6 km) centered around Southern California. From the 10-m MM5 wind speed, the wind stress has been calculated using Large and Pond (1981). From the time series of the wind stress τ_s in Fig. 2 it is clear that a couple of strong wind events (τ_s at least reaching up to 0.1 N/m^2) have occurred during the simulated period. The period from about December 2–8 with intermittently strong winds is followed by two distinct events of two to three days around the 10th and 15th of December. The second half of the month was less energetic with five shorter events reported. During the wind events the wind is mainly from westerly to northwesterly directions.

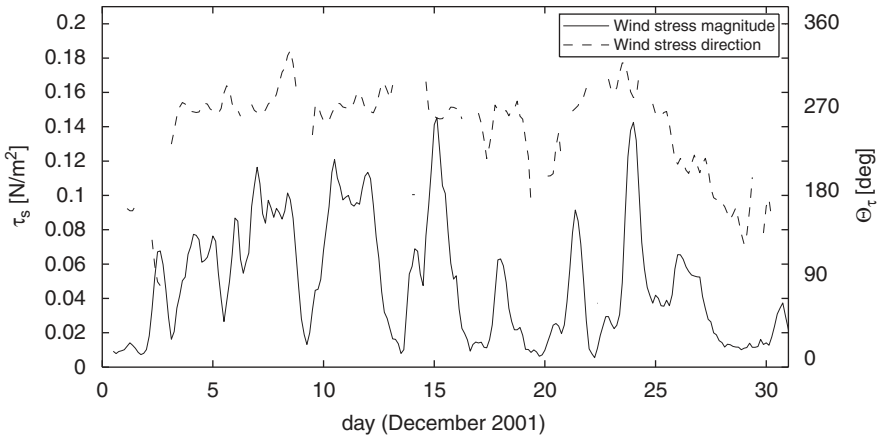

Fig. 2. Time series of three-hourly wind stress magnitude (τ_s, solid line) and direction (Θ_τ from where stress is directed, dashed) at the location of the NDBC wave buoy (33.85°N, 118.63°W), derived from the 6 km MM5 model. Time in days, December 2001, UTC. In the graph, the magnitude (direction) time series have been smoothed by a 12 (6) h moving average for clearer plotting; gaps in the direction appear when the vector passes through the North.

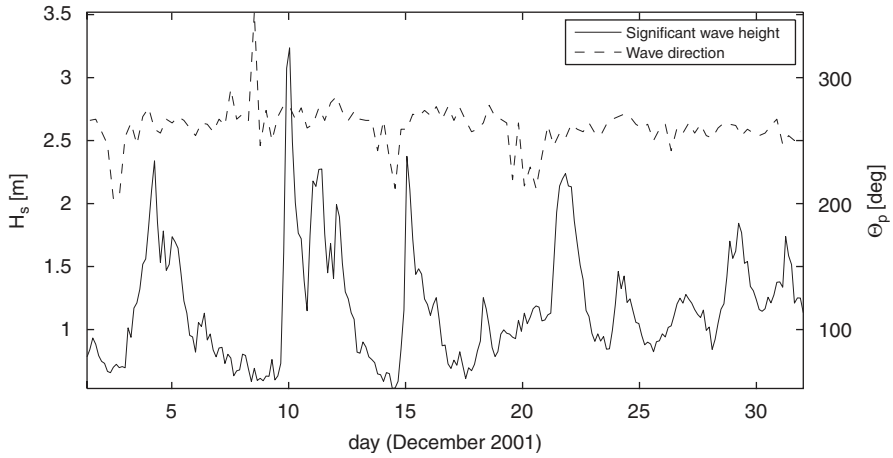

Fig. 3. Time series of three-hourly significant wave height (H_s, solid line) and peak direction (Θ_p, dashed) from the NDBC wave buoy (Buoy 46221, 33.85°N, 118.63°W, http://cdip.ucsd.edu).

3.5. Waves

To take into account the effect of the waves on the bottom stress, significant wave height, peak frequency, and peak direction are derived from an independent parametric swell-wave model by O'Reilly and Guza (1993). These quantities are used to calculate the bottom orbital velocity. The swell-wave model is a linear refraction–diffraction model, on the same grid and bathymetry as the innermost ROMS domain. It uses the observations from the SMB wave buoy (NDBC buoy 46221, 33.85°N, 118.63°W, http://cdip.ucsd.edu) to generate spatial fields of the required parameters. It should be noted that the direct application of these essentially monochromatic wave model results to compute near-bottom quantities leads to a bias when non-monochromatic waves are present in reality, as then the spectrum would redden towards the bottom (see Section 5).

In terms of wave conditions, the period of December 2001 is quite comparable to the months of December in the other recent years (http://cdip.ucsd.edu). Fig. 3 shows the time series of significant wave height H_s and peak direction Θ_p measured at the wave buoy. In the first half of the

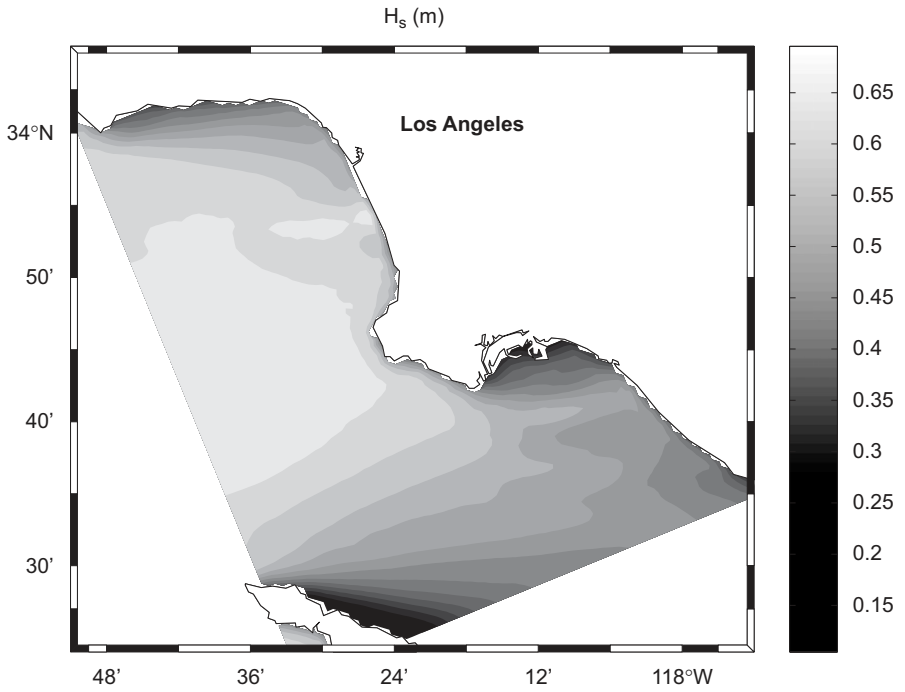

Fig. 4. Root-mean-square of significant wave height H_s from the SIO swell-wave model (O'Reilly and Guza, 1993) on the innermost ROMS domain over the period December 1, 2001 to January 1, 2001.

month three distinct wave events are visible. They coincide with the strong wind events of Fig. 2 except that the first wave event ends by December 5, whereas the period of intermittently strong winds continues. The December 10 wave event is the strongest, with $H_s > 3$ m. In the second half of the month the H_s peaks are smaller, and towards the end of the month, the relative influence of swell in the spectrum increases. Wave fields approach the area mostly out of south-westerly to westerly directions ($\Theta_p \approx 250^\circ$).

Fig. 4 shows the root-mean-square field of H_s from the simulated time period. It can be seen that on average the waves are higher in the SMB than in the SPB due to the sheltering effects of the PV peninsula and Catalina Island. Also, the relatively shallow and protruding plateau (''Short Bank'') in SMB can be seen to focus wave energy towards the center of the SMB and the central shore.

3.6. Sediment conditions

In all experiments, the same two size classes are considered: silt ($d_{silt} = 24\,\mu$m) and fine sand ($d_{sand} = 125\,\mu$m). This limits the computational effort and complexity of the analysis but retains information about differences depending on settling velocity and effects of bed composition and armoring. All experiments are initialized with an idealized sediment-bed composition. The initial distribution of the fractions ($f_{silt}, f_{sand} = 1 - f_{silt}$) is an analytical function of local depth h that approximates the observed features, i.e., sandy on the shelves and fining at larger depth towards a certain minimum value. Fig. 5 shows the spatial distribution of the initial silt fraction.

Settling velocity, entrainment rate and critical shear stress all are empirically related to grain size. Settling velocity w_s is computed from the empirical function of grain size by Soulsby (1997). The model input parameters are listed in Table 1. For all experiments sediment concentration c_j (mg/l), ripple length λ (m), and ripple height η (m) are each set to zero initially.

4. Results

In total four experiments are discussed: a control experiment and three experiments in which either armoring, ripple roughness or surface waves have been switched off.

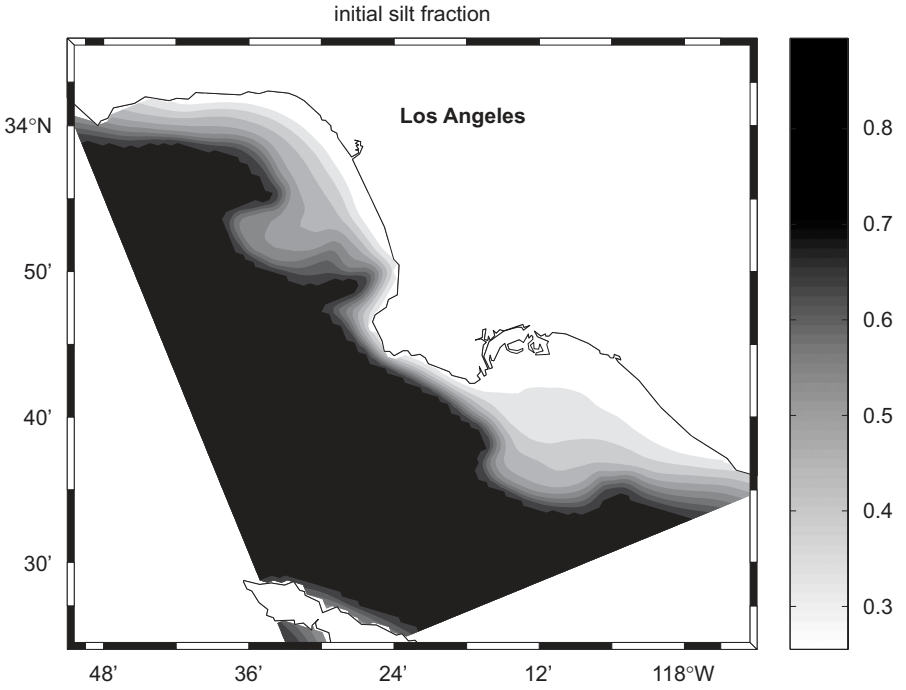

Fig. 5. Initial distribution of the silt fraction $f_{silt} = \max(\min[(h/h_{max})^{1/2}, f_{silt,max}], f_{silt,min})$, with $h_{max} = 200\,\text{m}$; $f_{silt,max} = 0.9$ and $f_{silt,min} = 0.25$, maximum and minimum silt fraction. Initial conditions are the same for both bed layers. The initial sand fraction is $f_{sand} = 1 - f_{silt}$.

4.1. Transport patterns

The control experiment includes all effects of waves, armoring, and ripple roughness. The results of this experiment suggest that the major resuspension events are closely tied to episodes with high waves (roughly $H_s > 1\,\text{m}$).

The mean flow in the channel between Catalina Island and the mainland is part of the California Current System. It drives the circulation in the bays by spinning up bay-size eddies that, at intervals of a few days, detach from the coast and migrate westwards. During December 2001 the simulated tidal-mean, depth-averaged flow through the channel is poleward with velocities of at most 5 cm/s, as is common in winter (Hickey, 1992). Depth-dependent tidal mean velocities are at most a few cm/s below 150 m, whereas above this level they increase up to 25 cm/s. This flow enters the domain at the southern edge and leaves either just north of Catalina Island or further north as it meanders when eddies in SMB develop and detach. Currents in the bay-size eddies are typically about 10 cm/s. These eddies are confined to approximately the upper 50–100 m. At depths below 200 m, an equatorward countercurrent is flowing through the channel, with maximum tide-averaged current speeds of about 10 cm/s at 400 m depth. An animation showing the depth-integrated silt concentrations is provided in the electronic supplement (Animation 1).

In general resuspension occurs in a few km wide strip along the coasts during the wave events. The sand is hardly transported by the currents, but the silt is advected along the coastlines at first (typically 10 to 20 km from the central erosion sites). Whenever a resuspension event lasts longer than about a day, the currents are able to carry silt out of the erosion areas in plumes. This is mainly the case in the first half of December 2001.

During this time of year all eddies that spin up in the SMB are anticyclonic. Hence, the plumes that are formed offshore of Santa Monica and El Segundo are generally advected along the coast towards PV peninsula after which they follow the coastline to the west and then either recirculate in the bay or enter the channel between Catalina and PV. In SPB the flow structures are often southeastward, such that plumes originating form the central nearshore zone off Seal Beach are advected

alongshore, southward towards the Newport Beach shelf break. Occasionally, the currents in SPB are divergent and a small part of the silts is transported northward towards PV. Those plumes subsequently move along the southeast shore of PV and sediments are carried into the channel and on the southwest facing slope of PV.

In general, it can be stated that it is the coincidence of high waves with eddies spinning up in the bays that causes sediment to be advected in plumes. Depending on the duration of the wind and wave event and the current speeds in the eddies, the silt is deposited either in the deeper parts of the bays or is ejected offshore into the channel. The difference between the first and second half of the month is the intensity and duration of the high wind and wave events, the later wave events are lower in magnitude, shorter in duration and more influenced by swell. As we will discuss in Section 4.5, the lower wind speeds imply less vertical mixing and, hence, lower concentrations of suspended sediments higher up in the water column where velocities are larger. Consequently, during the second half of the month resuspension occurs regularly (every time H_s in Fig. 3 exceeds a value of about 1 m), but large plumes, as in the first half of the month, do not occur, also because of the shorter duration of resuspension events.

Fig. 6a shows the vertically integrated silt concentration on December 15, 2001, about half a day after the peak in wave height of December 15. The depth-averaged, tidal-mean current velocities are also shown. Recently resuspended material in the shallow parts is clearly visible. This silt is partly advected along the coasts while resuspension continues. Offshore of PV, silt that has been transported offshelf during and after the previous event (December 10–12) is still visible. At the moment of the plot this plume remnant is at a depth of about 100 m below the surface.

The sand fraction is not transported in plumes during the December 2001 period, it is mainly moved around within the individual shelf areas over at most 1–2 km. The horizontal transport distances for sand are smaller due to the faster settling.

4.2. Bottom stress, ripples, and roughness

During the wave events the areas shallower than 20 m show clear resuspension but analysis of the wave–current bottom stress τ_{cw} in Eq. (A.2) indicates that the critical shear stress for silt $\tau_{cr,silt}$ is exceeded in areas down to about 50 m depth. This is consistent with the observational studies referred to in Section 1. Fig. 6b shows the percentage of time during the experiment that $\tau_{cw} > \tau_{cr,silt}$. In the areas between 30 and 50 m deep this occurs up to 20% of the time. Between 20–30 m the occurrence increases up to 70% of the time. In Fig. 6b it can also be seen that wave–current bottom stresses are relatively small offshore of the Los Angeles and Long Beach Harbors, an area that is partly sheltered from waves coming from the west and northwest. For the sand fraction, the percentage of time that $\tau_{cw} > \tau_{cr,sand}$ decreases more rapidly with depth than for the silt fraction, partly due to the nonlinear dependence of the wave-related stress τ_w on local depth in (A.3b). At 10–15 m, $\tau_{cw} > \tau_{cr,sand}$ more than 70% of the time, at 20 m depth this percentage is merely 30%.

Fig. 6c shows the ripple height (η) at the peak of the December 10 event as an illustration. Because of the initial plane bed conditions, bed forms will be found only there where bottom stresses have exceeded the critical value for ripple formation and the bed is predominantly sandy. Current-related ripples are found only in the deep parts of the Santa Monica and Redondo canyons. They develop in the first hours of the simulation and remain thereafter. Their height is about 0.4 mm and length is 3 cm. As can bee seen from Fig. 6c the wave-related ripple heights on the shelves range from 2 to 6 mm, typically increasing with increasing wave–current bottom stress. Ripple lengths vary from 2 to 5 cm, with similar patterns (not shown). When the stress exceeds the break-off limit, bed forms are effectively wiped out (see also Appendices A.1–A.2). This happens only during the peak of the December 10 event in exposed areas shallower than 15 m (i.e., around the moment of plotting in Fig. 6c, d). The effective roughness varies between 0.2 and 0.9 mm. The roughness includes ripple roughness and bed-load roughness, so that in the plane bed regime bed-load roughness compensates for loss of ripple roughness and the total roughness retains a value of about 0.8–0.9 mm.

4.3. Changes in bed thickness

The net effect of the successive resuspension, transport, and deposition over the month of December 2001 is displayed in the net change in bed thickness and silt fraction in the active layer in Figs. 6e and f, respectively. Most sediment is transported in the nearshore zones of less than

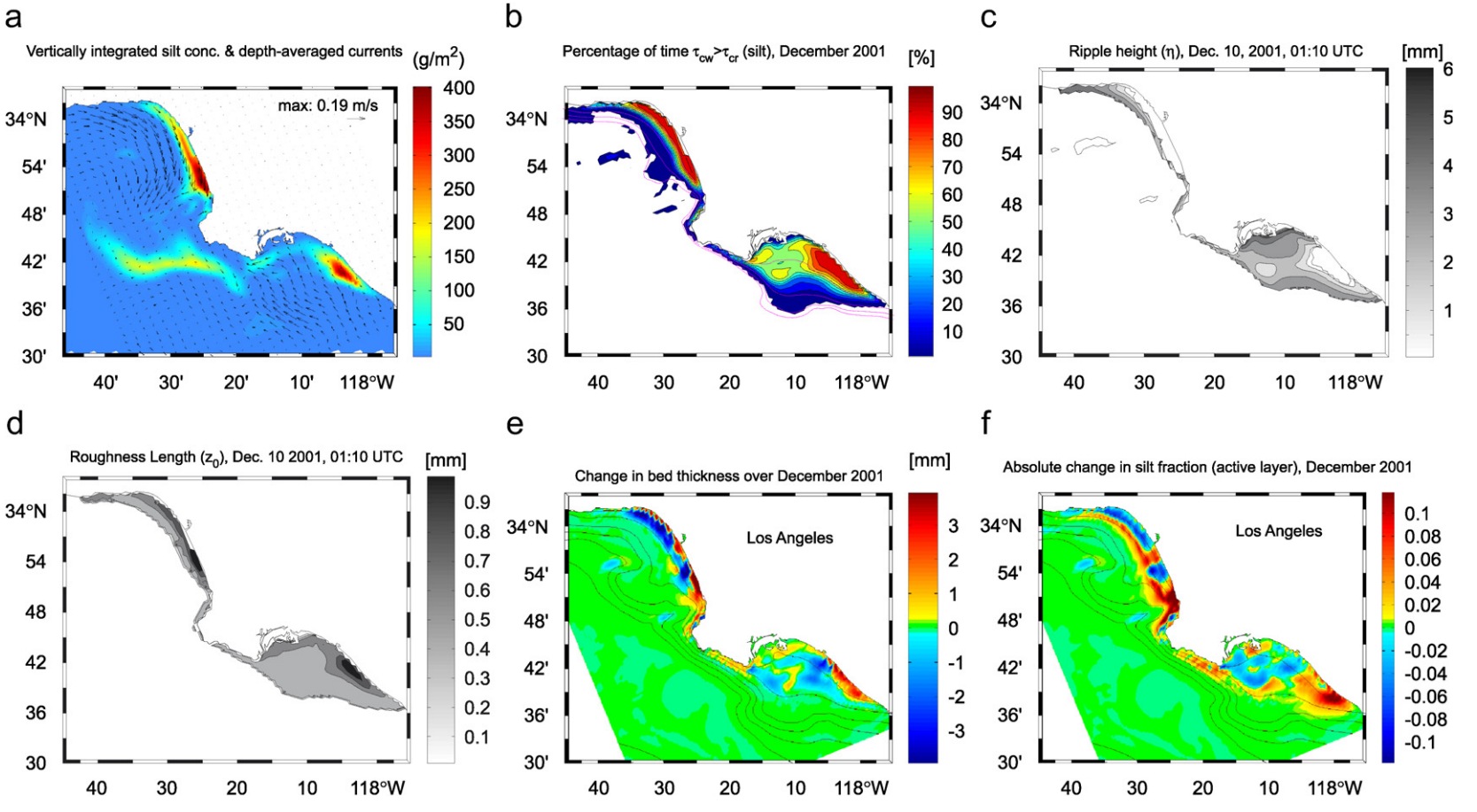

Fig. 6. (a) Depth-averaged, tide-averaged velocity and vertically integrated silt concentration, half a day after maximum of December 15 wave event. Concentrations locally up to 500 g/m^2. (b) Fraction of time that wave–current bottom stress exceeds the threshold for silt suspension, i.e., $\tau_{cw} > \tau_{cr,silt}$. Dotted lines: 20–65 m isobaths (15 m interval). (c) Ripple height (η) at the peak of 10 December wave event. (d) Bed roughness (including ripple roughness and bed-load roughness) at the peak of 10 December wave event. (e) Net change in bed thickness over December 2001 control experiment. Red: net deposition; blue: net erosion. Color range −4 to 4 mm, data range −28 to 11 mm (extremes just off Redondo Beach). Also shown are 15, 30, 60, 120, 240, 480 m isobaths. (f) As (e) but for net change in silt fraction of the active layer. Color range: −0.12 to 0.12, data range: −0.12 to 0.39 (extremes in nearshore areas).

30 m depth. Erosion is strongest in the area onshore of Short Bank where the wave height and fraction of time that $\tau_{cw} > \tau_{cr,silt}$ both attain a local maximum (Figs. 4 and 6b, respectively). In SMB the major depositional area is located directly at the shoreward end of the Redondo Canyon where the wave height has a local minimum. The erosion patterns are strongly tied to the wave height spatial distribution, whereas deposition is more determined by the dominant transport patterns during the wave events: the mesoscale circulation transports sand and silt towards the Redondo Canyon, where net deposition occurs. Part of the sediments pass this area and are deposited southwestward along the northern shore of PV. Finally a few percent of the silt mass is actually transported offshelf in the plumes.

In SPB the magnitudes of bed thickness change are lower (−4 to 4 mm) but the area where the bed is eroded is more extensive. Net erosion has occurred in the area off Huntington Beach, whereas deposition has taken place to the northwest (off Long Beach and Los Angeles Harbor) and southeast (off Newport Beach) of this area and in a local deposition area offshore. The northwestern deposition is related to the local decrease in wave exposure (Figs. 4 and 6b). The deposition in the center is due to a local increase in water depth (decrease in bed stress), whereas the deposition off Newport Beach occurs due to the advection along the shore during most events. This net deposition occurs despite the relatively larger exposure to waves in that area.

4.4. Changes in sediment size distribution

The differences in transport efficiency of the coarse and fine fraction are visible in the changes in silt fraction in Fig. 6f. In general, the shallowest areas of net erosion become coarser over time as silt is winnowed out of the bed. The adjacent deeper zones become finer, even when they are net erosional. In SMB, the strongest coarsening is found off El Segundo at the inshore side of the Short Bank, where also the strongest erosion occurred. The sorting patterns are consistent with observations by Edwards et al. (2003) who found a coarse area off El Segundo and fining in the Redondo Canyon. Observed conditions in the field, however, reflect the cumulative effect of multiple events of erosion and deposition, including external sources such as rivers that were omitted in the model. A one-to-one comparison of modeled and observed grain-size distributions would require a more comprehensive, longer-term simulation or event-scale observations.

4.5. Vertical concentration profiles

Fig. 7a illustrates the vertical structure of the silt concentration along transect S_1 (Fig. 1) through the plume offshore of Redondo Beach, three days after the maximum of the December 10 wave event. In the shallow areas concentrations increase monotonically with depth, but further offshore the vertical structure is non-monotonic indicating advection from inshore. The plume concentration at

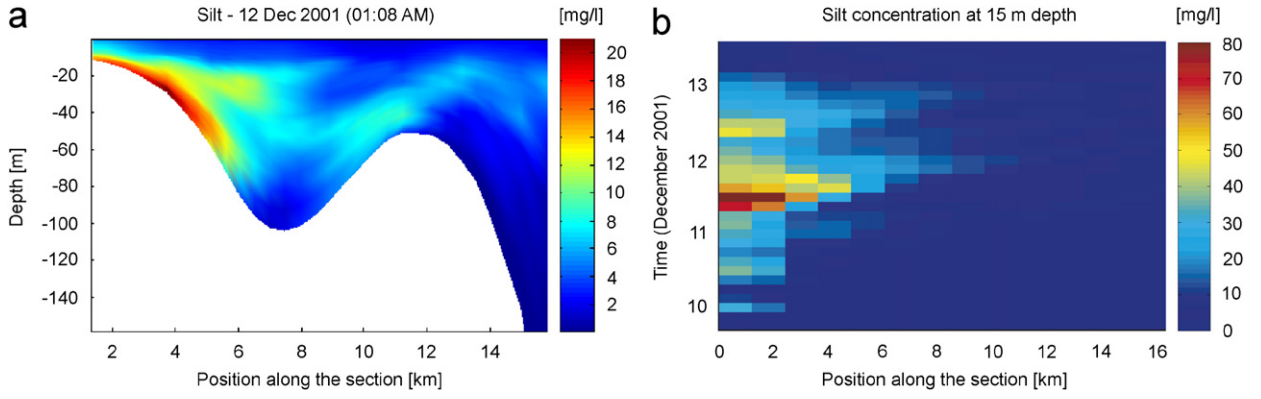

Fig. 7. (a) Vertical distribution of silt concentration along transect S_1 offshore of Redondo Beach to the southwest (Fig. 1) three days after the maximum of the December 10 wave event. (b) Hovmuller diagram of silt concentration at 15 m depth along the same transect over the entire December 10 wave event. The time resolution of the output is 3 h, the model time step was 30 s; the spatial resolution shown is the model resolution.

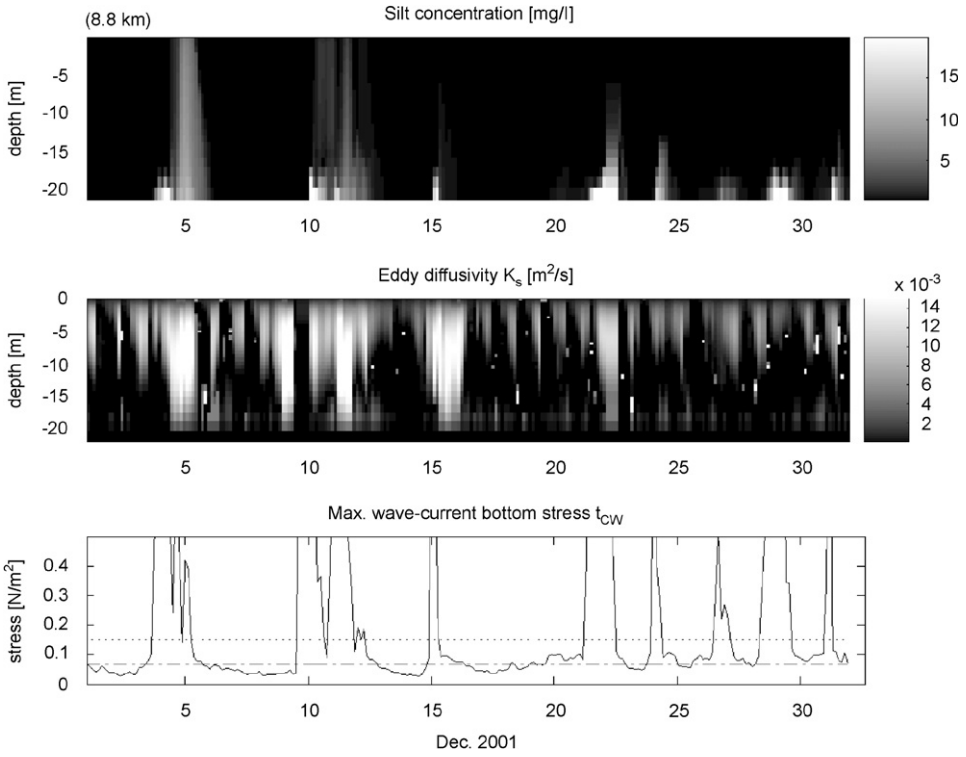

Fig. 8. Time evolution of vertical distribution of silt concentration c_{silt}, eddy diffusivity K_s, and maximum wave–current bottom stress τ_{cw} at location of asterisk on transect S_2 in Fig. 1 (118.21°W, 33.69°N). Dotted line in lower panel indicates $\tau_{cr,sand}$, dashed–dotted line $\tau_{cr,silt}$. Peaks of τ_{cw} reach up to 1–1.5 N/m^2 during the wave events, except for December 10 when stress peaked at 2 N/m^2.

20 m depth decreases rapidly offshore. The plume is capped by the surface mixed layer about 10 m thick. In the preceding days the plume has moved outward from the shelf as evident in the Hovmuller diagram of Fig. 7b. Note that in this location the maximum concentrations occur during the second peak of the wave height (December 11), whereas the waves were strongest on December 10. This is explained by the accumulation of resuspended silt in the water column over time and advection of silt from the main source area in the north. The maximum at 10 km offshore is found about half a day after the nearshore maximum, corresponding to an offshore transport speed of about 25 cm/s. Settling and advection continue for about half a day after the wave event is over, consistent with the settling velocity of 0.4 mm/s.

Fig. 8 shows the time evolution of silt concentration (c_{silt}), eddy diffusivity (K_s), and maximum wave–current bottom stress (τ_{cw}) at 8.8 km from the seaward end of transect S_2 over 22 m of water depth (n.b., the asterisk on S_2 in Fig. 1). Eight major silt resuspension events correspond to the eight most significant intervals of elevated H_s. From the bottom panel in Fig. 8, it can be seen that as soon as τ_{cw} exceeds $\tau_{cr,silt}$ it also readily exceeds $\tau_{cr,sand}$. The maximum stresses during the events are an order of magnitude larger than these critical stress values. As a consequence, the number of sand resuspension events is the same as the number of silt events but the duration is shorter. The major difference between sand and silt is found in the vertical profiles. Sand is mostly confined to the lowest meter, whereas silt is resuspended well into the column when K_s is large over the entire column.

The middle panel of Fig. 8 shows that eddy diffusivity K_s has a local minimum in mid-column for most of the time. K_s in the bottom layer varies over time with the tidal currents and waves whereas effects of diurnal cycle of heating–cooling and—related to that—wind stress (sea breeze) can be seen in the surface layer. During the wind events in the first half of the month and on December 22 and 24, the surface layer deepens. During the wave events the bottom boundary layer height increases as well. In the first half of the month the values of surface and bottom boundary layers both overlap and silt is brought well up into the water column.

The coincidence of enhanced resuspension due to waves, and surface mixing significantly facilitates lateral sediment-transport. Concentrations at mid-column are an order of magnitude higher than when resuspension does not coincide with surface-enhanced vertical mixing, as can be seen at the end of the month. The final three wave events of December are swell-dominated and do not coincide with very high winds. Sediment is resuspended, but it does not extend beyond a layer of a few meters thick.

Fig. 9 further illustrates the differences in the bottom stress and vertical mixing between the first and second half of the month along transect S_2 (see Fig. 1). The upper panel shows $\tau_{cw} > \tau_{cr,silt}$, the lower panel shows the instances when the surface and bottom layers overlap and indicates which of the layers is the deepest. Offshore of 4 km (40 m depth), no resuspension occurs, and offshore of 6 km (25 m depth), the mixing layers never overlap. The closer to shore, the more extensive the resuspension and the more frequently the layers overlap. Also, the more onshore, the more the overlap is determined by the bottom boundary layer. The vertical sediment profiles vary accordingly: at 26 m depth resuspension is confined to the lower 5 m whereas at 17 m depth five out of eight events show vertical mixing of silt over the entire column. In the most nearshore part of the transect (12 m depth), all events result in silt mixed over the entire column. Nevertheless, even in these shallow areas, resuspended sand is found only in a 1–2 m thick bottom layer, because of its high settling velocity .

4.6. Sensitivity to ripple roughness, armoring, and waves

In three sensitivity experiments the effects of ripple roughness, armoring, and waves on the sediment erosion and transport are evaluated. The first two experiments involve empirical parameterizations that may depend on site conditions. The ripple parameterizations (Appendix A.2) have been derived for sandy beds and are as yet untested for the mixed silt–sand conditions on the Southern California shelves. Recent sea floor observations (Xu, 2005), for example, suggest that, at least in one particular nearshore area in SPB, ripples are non-orbital in their structure rather than the more common orbital ripples as parameterized here. Neither has the armoring parameterization been assessed under typical conditions for SMB and SPB. For both parameterization validations, a more

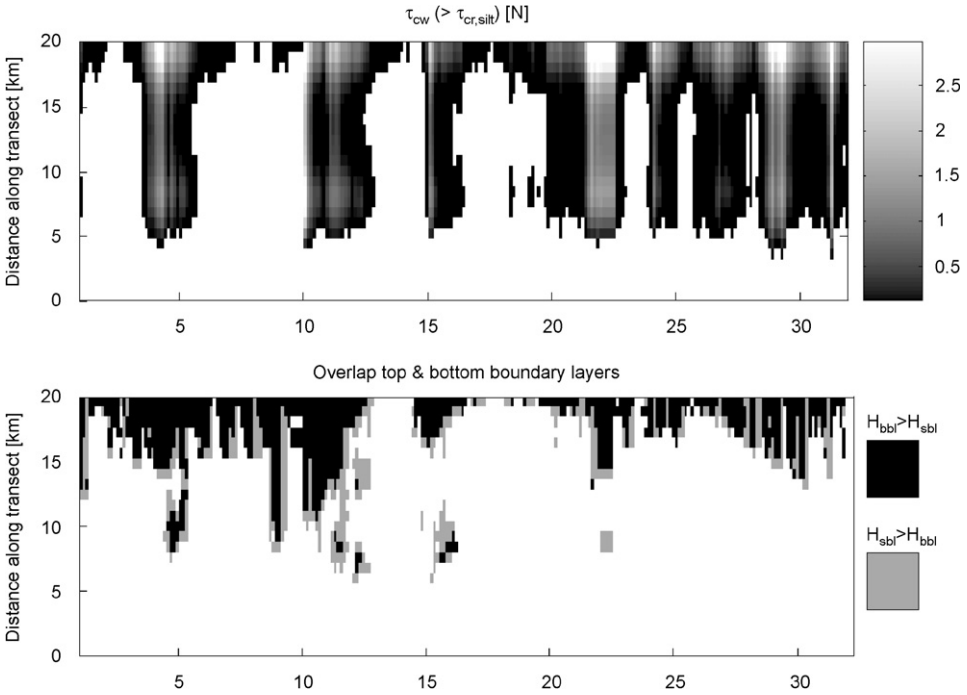

Fig. 9. (top) Hovmuller diagram of maximum wave–current bottom stress τ_{cw} along transect S_2, shown only when exceeding the critical shear stress for silt erosion. (bottom) Hovmuller diagram showing instances when both surface and bottom boundary layers overlap (black: bottom layer thickness H_{bbl} exceeds surface layer thickness H_{sbl}; gray: vice versa; white: layers do not overlap).

extensive data-model comparison study would be required in future. As a third sensitivity experiment, the surface waves were excluded while retaining the bed-load, ripple roughness, and armoring, so that sediment is set into motion by the currents alone. This gives insight into the importance of the surface waves and the potential for currents to resuspend sediments.

No ripple roughness: The ripple roughness parameterization determines the effective bed roughness length and hence the bottom shear stresses. In the first experiment, the effects of ripples on the roughness length z_0 has been ignored. Bedload roughness has still been taken into account. The time evolution of the vertically integrated concentrations does not differ significantly compared to the control run. Also the patterns of net erosion and deposition as shown in Fig. 6c remain qualitatively the same because the maximum wave–current stress, responsible for sediment resuspension, depends on skin friction and bed-load roughness only. The mean wave–current stress—relevant for the momentum equations and vertical diffusion—does depend on ripple roughness: with ripples, stresses on the shelf are up to 100% stronger during wave events than without ripples. During calm periods the ripples enhance the stress by about 20%, because the ripples have become smaller then.

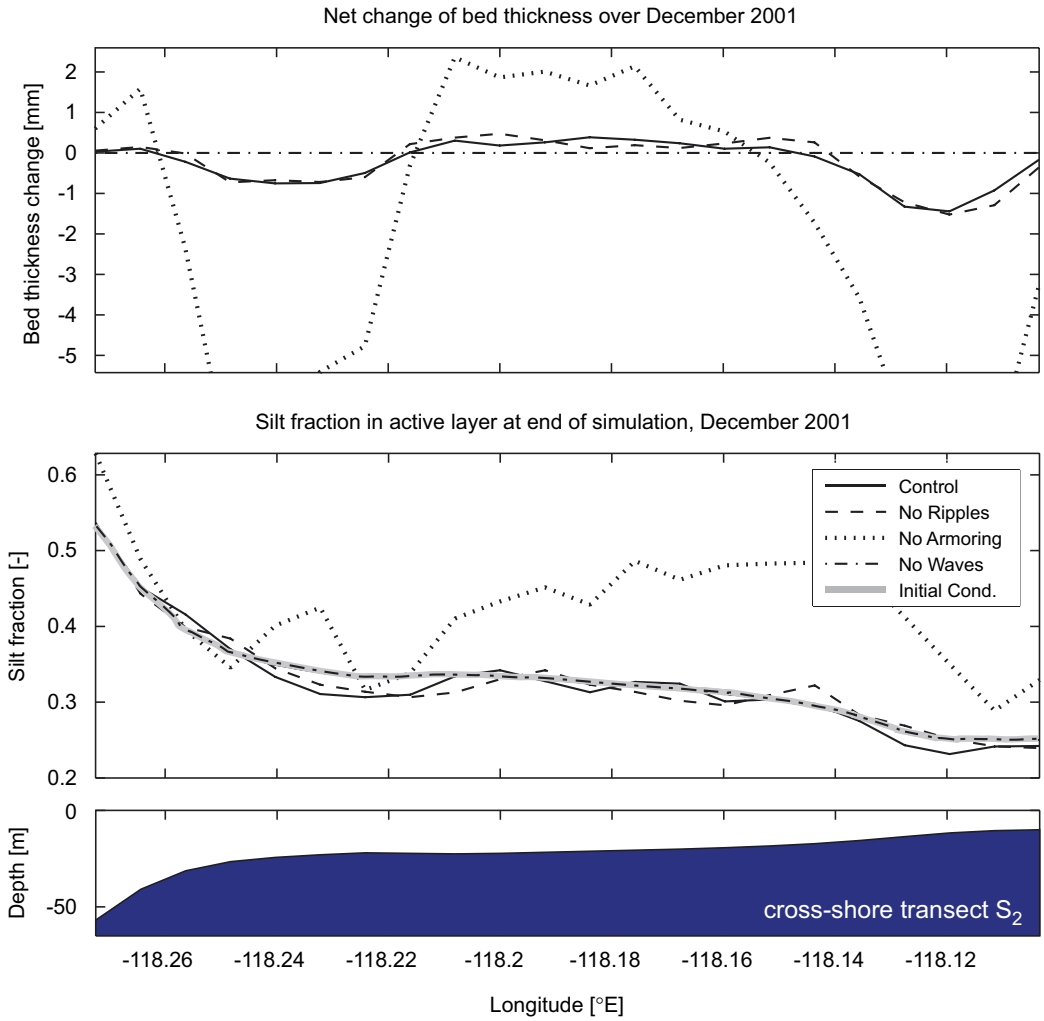

Fig. 10. Changes in the bed along transect S_2 (offshore to onshore across SPB, see Fig. 1) at the end of the control and three sensitivity experiments. Top: net change of bed thickness (positive net deposition and vice versa). Middle: silt fraction in the active layer of the bed at the end of the simulation (initial silt conditions are shown as a gray line). Bottom: depth along the transect. Mean silt transports during December 2001 are from right to left.

Depth-averaged currents on the shelf are generally 10–20% lower and K_s values in the bottom boundary layer are about 10–20% higher when ripples are activated.

The influence of these changes in flow and mixing on the net sediment-transports can be seen in Figs. 10 and 11 which show the net changes in bed thickness and silt fraction over the simulated period along transects S_2 and S_3 for this and the other sensitivity experiments. The largest differences in thickness are found in the nearshore areas and are at most about 2.5 mm. On average the differences are less than tenths of mm. Turning off the ripple roughness increases the local gradients in the bed thickness: deposition occurs closer to the erosional spots, suggesting smaller transport distances. This is confirmed by the changes in bed composition: erosional areas are slightly more silty. When ripples are neglected, transporting currents may be less damped by bottom friction, but the vertical resuspension height is lower. The net result is a smaller transport distance. However, the changes are very small and difficult to discern during individual events.

No armoring: The effect of neglecting bed armoring (i.e., replacing (3) by $E_0 = E_u$) is clearly seen in the net erosion and deposition. Figs. 10 and 11 show that the erosion and deposition increase significantly when armoring is switched off. Especially, the erosion is more pronounced: in the control experiment a few mm of the bed were removed, now an unrealistic amount of tens of mm is eroded. This material is deposited mainly in the Redondo Canyon, along the Northwestern PV

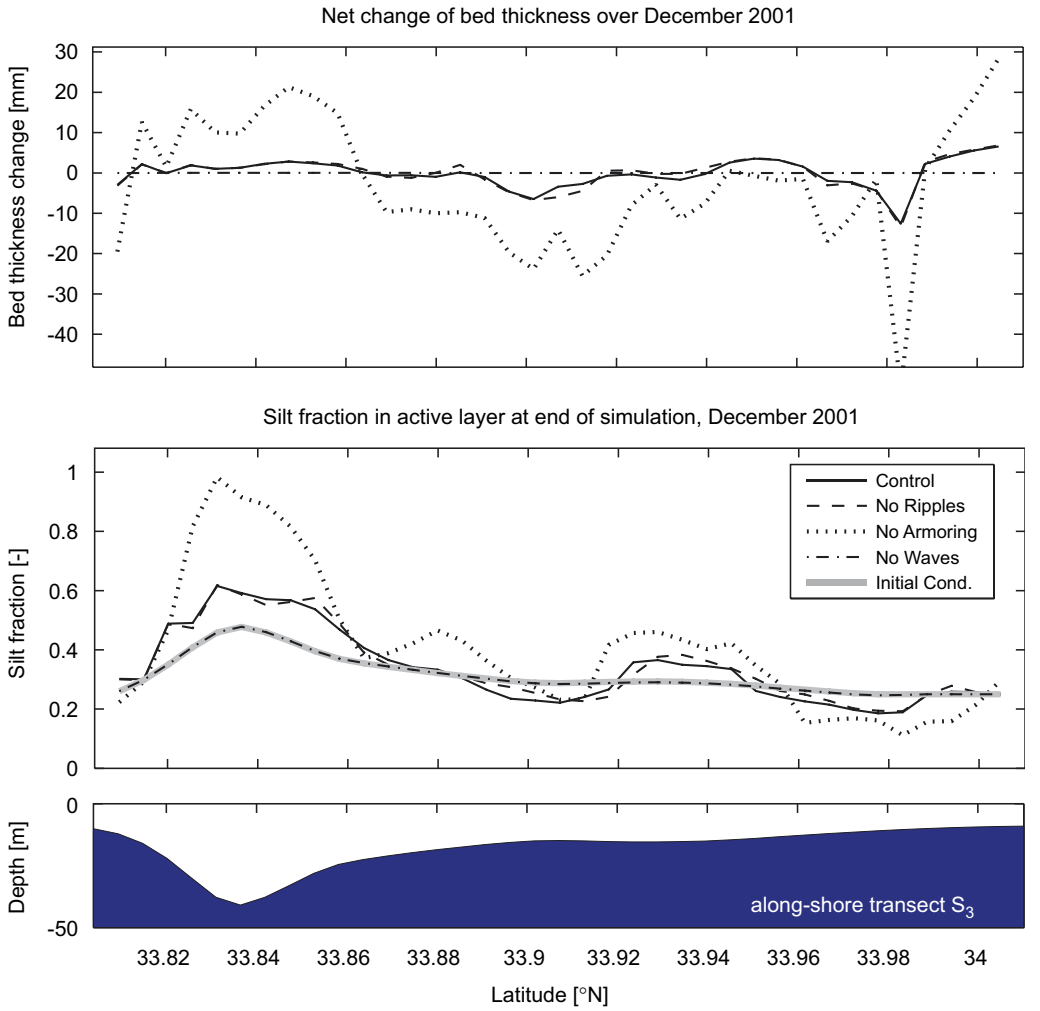

Fig. 11. As Fig. 10, but for transect S_3 (south–north along the shore of SMB). Here also the mean silt transports during December 2001 are from right to left. Minimum values in top panel are −6 and −7.7 mm, respectively.

coast, off the LA and LB Harbor, off Newport Beach. On transect S_2 in SPB the silt fraction is increasing overall, even in the erosive areas, because over the whole shelf, the lower water column becomes filled with suspended silt. In the SMB however, gradients increase: the silty Redondo Canyon area (the depression on S_3) becomes more silty, and the sandy inner shelf off Santa Monica (the shallowest area on S_3) becomes more sandy, since winnowing of silt from the shallow areas continues more strongly than it would with armoring. Due to deactivating armoring, the silt concentrations are approximately 20 times larger near the bottom and about 10 times larger higher in the water column. Sand concentrations are about 5 times larger overall. Armoring thus has the strongest effect on the erosion and transport of the silt fraction. This is consistent with results from 1- and 2-D models by Wiberg et al. (1994), Reed et al. (1999), and Harris and Wiberg (2002).

No waves: Among the three sensitivity experiments, the waves have the greatest consequences for the amount of sediment moved, as might be expected from the control experiment. Also, earlier studies indicated the dominance of waves on Californian shelves (Drake and Cacchione, 1985; Wiberg et al., 2002). The bottom stresses when waves are absent only occasionally exceed the threshold level for silt, and virtually never exceed that for sand. The little erosion that takes place on the shelves is related to flow acceleration around headlands and inside canyons. Erosion is seen around the corners of the PV peninsula and off Point Dume at the northwestern edge of the SMB. On all these occasions the total net erosion/deposition is of the order of 0.01 mm, two orders of magnitude smaller than the shelf erosion in the control experiment. Other scouring spots are found in the Santa Monica and Redondo Canyons. These develop due to strong near-bottom tidal currents accelerating through these topographic contractions. It should be remarked that both horizontal and vertical model resolutions are limited at these canyons. The results on these locations must therefore be regarded with care, pending a more refined grid for a detailed study in the canyons.

5. Discussion

The main point of discussion is how to validate the model and relate the results to realistic circumstances. Within the limitations of our numerical resolution, we have acquired some confidence in the model performance. A necessary next step is to more quantitatively test the currents, wave motions, stresses, mixing parameterizations, and sediment parameters calibrated. Nevertheless, the present model—supplied with sediment parameter values from the literature and tidal, wind, and wave forcings from independent models and without any data assimilation and with very little tuning—already shows encouraging results. Although freshwater discharges and organic sources of suspended matter are lacking, the subsurface silt plumes have similar extent and spatial and temporal evolution as the buoyant satellite-observed plumes by Nezlin and DiGiacomo (2005). This supports the representation of the dominant mesoscale transports. As discussed in Section 3.3, the tidal and subtidal currents also have the right magnitude, at least at the offshore mooring location available to us. Typical combined wave–current bottom stresses in SMB compare well to measured stresses at 35 and 70 m depth in the middle of SMB (Noble and Xu, 2003), although the presently configured model does not exhibit the intermittent variability that Noble and Xu attribute to internal waves. Therefore, we cannot assess hypotheses relating internal wave breaking to anomalous shelf-break erosion.

Since surface waves are so significant for resuspension, next steps should certainly include further improvements in the wave modeling. Instead of an offline swell-wave model for the dominant wave components, we wish to include a more complete wave spectrum, local wind generation, and coupled wave–current interactions by shoreline wave breaking and the vortex force (McWilliams et al., 2004). In this study, we treated the wave field as an equivalent monochromatic wave with a peak period obtained from the wave-model surface field. Because attenuation of lower frequency waves with depth is less compared to the higher frequencies, the spectrum at the sea floor will be redder. Harris and Wiberg (2001) and Xu (2005) indicate that taking into account the different attenuation of low- and high-frequency waves may be especially relevant for sediment motion.

The choice for our values of entrainment rate E_u is only weakly justified from measurements. They have been set to obtain concentrations of realistic general order of magnitude (cf., Drake and Cacchione, 1989; Xu et al., 2002). As shown by our armoring sensitivity experiment, the composition of the bed does influence the fluxes and effective

roughness. Hence, for more realistic quantitative experiments, representative erodibilities must be established from in situ observations. Then, we may need to extend the present model with more size classes for a good reproduction of field data, as for example was also needed by Wiberg and Harris (2002). And we will further explore the sensitivity of the results to the armoring parameters. For now we have adopted the literature values by Garcia and Parker (1991), but a brief senstivity test showed that especially the bed composition is sensitive to active-layer thickness (over 50% change in silt fraction for a doubling/halving of δ_a) and the amount of erosion is very sensitive to the powers and coefficients in Eq. (3) (e.g., over 100% change in erosion when $\lambda_E = 1 - 0.5\sigma_\phi$ instead of $\lambda_E = 1 - 0.29\sigma_\phi$).

Our present choice of one silt and one sand fraction is illustrative but cannot be a full representation of the wide grain-size variation on the Southern Californian shelves. Also, the initialization of the sediment bed can be made more realistic, either incorporating measurements and/or spinning up the model for much longer time in sediment-transport mode to enable the bed to reach a (quasi-) equilibrium with prevailing conditions.

Nevertheless, the results show the importance of the vertical mixing for the horizontal transports of suspended sediments. This extends the conclusions of Warner et al. (2005) to realistic shelf-sea conditions. Warner et al. (2005) found that the development of an estuarine turbidity maximum in a model depends crucially on the parameterization of vertical mixing. Here we show that the extent of vertical mixing, together with the sub-tidal flow conditions, determines the horizontal transport ranges on the larger scales of shelves and bays. We deliberately chose to limit ourselves to the KPP scheme coupled to the wave–current bottom stress. The performance of KPP in the bottom boundary in the present application seems reasonable, but it requires further validation from field data of not only passive dissolved materials but also suspended solids. (Recently, the same KPP scheme has been successfully applied in ROMS to reproduce tidal mixing fronts off the coast of Brest, France (Cambon, 2005)).

6. Conclusions

The recently developed sediment-transport capabilities within ROMS have been applied to simulate transport on the shelves of SMB and SPB. The chosen period (December 2001) is dominated by events of high waves and mesoscale eddies. Under these circumstances local waves are the most important trigger for resuspension. Erosion patterns reflect the patterns of wave orbital velocities, which are determined by coastal geometry and direction of the wave fields. Erosion is strongest in nearshore zones of a few km wide, form where plumes of silty sediments develop. The transport patterns mostly reflect the mesoscale flow patterns during the simulated period, viz., anticyclonic bay-size circulations in SMB and often dipole-like flow structures in SPB. The currents are capable of transporting the silt fractions off shelf especially when vertical mixing is strong. Canyons are able to trap part of the silt transported alongshore.

The combination of enhanced bottom stress and wind mixing is important. When the surface and bottom mixed layers overlap, the silts can be further suspended instead of remaining in the bottom layer of a few meters thick. As the current velocities are larger up in the water column, the coincidence of strong winds and waves creates the best potential for long-distance transport. For the sandy fraction, the mixing is less relevant as most sand settles too fast to be transported offshelf within any single event.

The patterns of grain sorting are qualitatively consistent with field observations: coarsening close to shore (in particular where wave rays are focused) fine material trapped in the canyons.

Accurate wave modeling is essential for realistic sediment-transport predictions. Without waves even the fine fraction in the model is hardly suspended. The sensitivity experiments show that the direct influence of additional ripple roughness on erosion and deposition is relatively weak.

Switching off bed armoring locally results in a relatively strong increase of near-bottom concentrations of a factor of 20 for silt and a factor of 5 for sand because the supply of silt now is no longer limited in erosive areas. The net effect is more pronounced erosion and deposition zones, and stronger spatial gradients in grain-size distribution. The effect of bed armoring is larger than the effect of (uncertainty in dimensions of) ripples.

In summary, the present model seems ready as a useful tool for supporting more quantitative measurements of sediment movement on Southern California shelves.

Acknowledgments

This publication was supported in part by the National Sea Grant College Program of the U.S. DoC's National Oceanic and Atmospheric Administration under NOAA Grants #NA06RG0142 and #NA04OAR4170038, project #RCZ-171, through the California Sea Grant College Program; and in part by the California State Resources Agency. The views expressed herein do not necessarily reflect the views of any of those organizations. Further support came from Orange County Sanitation District and U.S. Geological Survey Cooperative Agreement, Award #04WRAG0048. The authors thank Bill O'Reilly (SIO) for providing the wave model data. Discussions with Chris Sherwood, John Warner, and Hernan Arango on the development of the sediment-transport and bottom stress routines have been very fruitful. M.B. appreciates the hospitality of the Institute of Marine and Atmospheric research (IMAU) at Utrecht University and in particular the interest of Huib de Swart. We are indebted to Alexander Shchepetkin for his work on ROMS algorithms, in particular the super-Courant settling scheme.

Appendix A. Bottom stress and related processes

A.1. Combined wave–current bottom stress

The wave-averaged, combined wave–current bottom stress is expressed as function of τ_w and τ_c (i.e., the stress due to waves in the absence of currents and due to currents in the absence of waves, respectively) according to Soulsby (1995):

$$\bar{\tau}_{cw} = \tau_c \left[1 + 1.2 \left(\frac{\tau_w}{\tau_c + \tau_w} \right)^{3.2} \right]. \quad \text{(A.1)}$$

The maximum wave–current shear stress within a wave cycle is obtained by adding $\bar{\tau}_{cw}$ and τ_w (with φ_{cw} the angle between current and waves):

$$\tau_{cw} = \left[(\bar{\tau}_{cw} + \tau_w \cos \varphi_{cw})^2 + (\tau_w \sin \varphi_{cw})^2 \right]^{1/2}. \quad \text{(A.2)}$$

The stresses τ_c and τ_w are determined using:

$$\tau_c = \rho \left(\frac{\kappa}{\ln(z_a/z_0)} \right)^2 u^2|_{z=z_a}, \quad \text{(A.3a)}$$

$$\tau_w = \tfrac{1}{2} \rho f_w u_b^2. \quad \text{(A.3b)}$$

Here $\kappa = 0.4$ is the Von Kármán constant, and $z = z_a$ is the reference height above the bed; u_b is the bottom orbital velocity which is determined from the significant wave height H_s, peak frequency ω_p; $f_w = 1.39(u_b/\omega_p z_0)^{-0.52}$ is a wave-friction factor according to Soulsby (1995).

The wave orbital velocity u_b is determined using Airy wave theory:

$$u_b = \omega_p H_s / 2 \sin \mathrm{h}(kh), \quad \text{(A.4)}$$

with h the local depth and k the local wave number from the dispersion relation, $\omega_p^2 = gk \tan \mathrm{h}(kh)$. The wave field is treated as monochromatic with amplitude half H_s and peak period.

The wave–current interaction in the bottom boundary layer is taken into account only if $u_b > 1\,\mathrm{cm/s}$; otherwise, current-only conditions apply. Given the grain size distribution in the active layer, the representative critical stress τ_{cr}, settling velocity w_s and density ρ_s are determined. To determine the shear stress relevant for sediment resuspension and the roughness length due to bed forms, we follow the concept of Li and Amos (2001) briefly summarized here.

First, the skin stresses for current-only and wave-only conditions are computed from the equations above, using the Nikuradse roughness $z_0 = d_{50}/12$, where d_{50} is the median grain size in the active layer. A bed-load layer develops as soon as the maximum wave–current skin friction $\tau_{cw(skin)}$ exceeds the critical stress τ_{cr}. This layer affects the stress effective for ripple formation and sediment resuspension. We adopt an empirically determined bed-load roughness $z_{0(bedload)}$ (Li and Amos, 2001):

$$z_{0(bedload)} = 17.4 d_{50} \left(\frac{\tau_{cw(skin)} - \tau_{cr}}{(\rho_s - 1) g d_{50}} \right)^{0.75}, \quad \text{(A.5)}$$

which yields values up to at most 0.9 mm during the strongest wave event (see Section 4.2).

A.2. Ripples

The bed-load roughness determined above is used in Eqs. (A.1)–(A.3b) to determine the maximum wave–current bed-load stress $\tau_{cw(bedload)}$ that is relevant for sediment resuspension and bed forms. Subsequently, for sandy locations ($d_{50} > 63\,\mu\mathrm{m}$), ripple height η and length λ are computed following Li and Amos (2001). Different ripple regimes are found for increasing stress: no-transport regime, local-transport regime, equilibrium regime, break-off regime, and upper-plane bed conditions.

Once ripple height and length are known, ripple roughness is determined using Grant and Madsen (1982): $k_b = 27.7\eta^2/\lambda$, $z_{0(rip)} = k_b/30$. This is used in

(A.1)–(A.3b) to obtain $\bar{\tau}_{cw(rip)}$ which determines the drag on the flow and provides the shear velocity for the KPP scheme. In the case where waves are not considered, the current-related ripple roughness is determined using the expressions for ripple length and height from Yalin (1964) and Allen (1970), respectively: $\lambda = 1000 d_{50}, \eta = 7.4(\lambda/100)^{1.19}$. Once the ripple roughness is known, (A.3a) determines the drag on the flow and friction velocity appropriate for the computation of the vertical eddy diffusivity and viscosity (see next section).

A.3. K-profile parameterization (KPP)

The KPP scheme (Large et al., 1994) parameterizes the vertical turbulent fluxes of scalars and momentum in terms of K-closure of turbulent fluxes: $\overline{w'a'}(z) = -K_a(\partial a/\partial z - \gamma_a)$, where primes indicate turbulent quantities; w is the vertical velocity; a is any scalar quantity or horizontal velocity component; and K_a is the vertical eddy diffusivity or eddy viscosity. The non-local transport term γ_a is non-zero only in the convective surface layer, and it is neglected for the bottom layer. In addition to the original paper by Large et al. (1994) describing the surface boundary layer, we now have applied the same principles to the bottom boundary layer, including the link to wave–current enhanced bottom stress. Below, the main features and dependencies of the parameterization are summarized for both surface and bottom layer.

In the stratified interior, K_a is determined by superposition of internal wave breaking, vertical shear instability and double diffusion: $K_a = K_a^w + K_a^s + K_a^d$. Double diffusion is not considered relevant for the area of interest, so $K_a^d = 0$. Internal wave breaking is parameterized according to Garrett and Holloway (1984): $K_a^w = \alpha/N$, with a lower bound to the buoyancy frequency N^2 of $10^{-7}\,\mathrm{s}^{-1}$ and $\alpha = 10^{-7}$ for scalar and $10^{-6}\,\mathrm{m}^2\,\mathrm{s}^{-1/2}$ for momentum mixing. Mixing due to vertical shear is a function of the local gradient Richardson number Ri_g. The shear-related mixing coefficients are determined by

$$K_a^s = K_0 \quad \text{for } Ri_g < 0, \tag{A.6a}$$

$$K_a^s = K_0[1 - (Ri_g/Ri_{g,c})^2]^3 \quad \text{for } 0 < Ri_g < Ri_{g,c}, \tag{A.6b}$$

$$K_a^s = 0 \quad \text{for } Ri_g > Ri_{g,c}, \tag{A.6c}$$

with $Ri_{g,c} = 0.7$, $K_0 = 50 \times 10^{-4}\,\mathrm{m}^2\,\mathrm{s}^{-1}$ and $Ri_g = N^2/((\frac{\partial u}{\partial z})^2 + (\frac{\partial v}{\partial z})^2)$. Under statically unstable conditions a convective mixing coefficient $K_a^c = 0.1\,\mathrm{m}^2\,\mathrm{s}^{-1}$ is added: $K_a = K_a^w + K_a^s + K_a^c$.

In the surface and bottom layers the mixing coefficient is determined by the boundary layer thickness H_{bl}, a depth-dependent turbulent velocity scale w_a, and a non-dimensional shape function G: $K_a(\sigma) = H_{bl} w_a(\sigma) G(\sigma)$, where $\sigma = \tilde{z}/H_{bl}$ is the non-dimensional boundary layer coordinate, directed towards the interior ($0 < \sigma < 1$); w_a, H_{bl}, and G depend on boundary forcing (buoyancy and shear stress) and stability of the boundary layer as outlined below.

The turbulent velocity scale w_a is given by

$$w_a = \frac{\kappa u_*}{\phi_a(\varepsilon H_{bl}/L_{MO})} \quad \text{for } \varepsilon < \sigma < 1 \text{ and } L_{MO} < 0, \tag{A.7a}$$

$$w_a = \frac{\kappa u_*}{\phi_a(\tilde{z}/L_{MO})} \quad \text{otherwise}, \tag{A.7b}$$

with $\varepsilon = 0.1$ the fraction of the boundary layer where Monin–Obukhov similarity applies (i.e., the surface layer) and ϕ_a the associated stability function. $L_{MO} = \frac{u_*^3}{\kappa B_f}$ is the Monin–Obukhov length scale. In unstable conditions, the profile velocity scale is kept at its $\sigma = \varepsilon$ value outside the surface layer (cf., (A.7a)). The friction velocity u_* and buoyancy flux B_f are defined at the outer boundary. At the surface u_* is derived from the applied wind stress: $u_* = \sqrt{\|\tau_s\|/\rho}$; at the bottom the combined wave–current stress averaged over the wave period is used: $u_* = \sqrt{\|\bar{\tau}_{cw(rip)}\|/\rho}$. The buoyancy flux at the bottom boundary is zero (so $w_a = \kappa u_*$).

The boundary layer thickness H_{bl} is determined using a bulk Richardson number (Ri_b) such that H_{bl} equals the smallest z value where $Ri_b = Ri_{b,c} = 0.3$, with

$$Ri_b(\tilde{z}) = \frac{\Delta B(\tilde{z})\tilde{z}}{(\Delta V(\tilde{z}))^2 + V_a^2(\tilde{z})}, \tag{A.8}$$

where ΔV and ΔB are the absolute differences between near-boundary and local velocity and buoyancy, respectively, and V_a is the velocity scale of the turbulent shear, defined by

$$V_a^2(\tilde{z}) = \frac{N w_a C_v}{\kappa^2 Ri_{b,c}} \left(\frac{-\beta_T}{c_s \varepsilon}\right)^{1/2} \tilde{z}, \tag{A.9}$$

where $C_v = 1.8$, $\beta_T = -0.2$, $c_s = 99.0$. Under conditions of weak stratification, the bottom-layer depth is limited by the Ekman depth, $H_E = 0.7 u_*/f$.

The profile of K_a in the boundary layers is given by shape function $G(\sigma)$, a cubic polynomial

determined by matching the mixing coefficients and their first vertical derivatives to the surface layer values at $\sigma = 0$ and to the interior values at $\sigma = 1$ (see for details Large et al., 1994). During the KPP computation, first the interior values of K_a are determined for the entire column, then boundary layer thickness, w_a, and $K(z)$ profiles for both layers are determined. Where both layers overlap, the larger of the two K values is retained so that a continuous $K(z)$ profile results.

Appendix B. Supplementary data

Supplementary data associated with this article can be found on the online version at 10.1016/j.csr.2006.12.003.

References

Allen, J.R.L., 1970. Physical Processes and Sedimentation. Unwin University Books, London.

Ariathurai, R., Arulanandan, K., 1978. Erosion rates of cohesive soils. Journal of Hydraulic Division ASCE 104 (2), 279–282.

Blayo, E., Debreu, L., 1999. Adaptive mesh refinement for finite-difference ocean models: first experiments. Journal of Physical Oceanography 29 (2), 1239–1250.

Cambon, G., 2005. Transport processes in tidal seas: example of the Ouesant front. Technical Report, Brittany Region Annual Report, Brest, France.

Colella, P., Woodward, P.R., 1984. The piecewise parabolic method (PPM) for gas-dynamical simulations. Journal of Computational Physics 54, 174–201.

Conil, S., Hall, A., Ghil, M., 2007. Wind regimes in Southern California winter. Geophysical Research Letters, in revision.

Da Silva, A., Young, C., Levitus, S., 1994. Atlas of surface marine data 1994. Technical Report, vol. 1–5, NOAA, Washington DC, USA. Atlas NESDIS, pp. 6–10.

Dong, C., Hall, A., Hughes, M., McWilliams, J.C., 2007. Impact of wind resolution on simulation of a major coastal upwelling event, submitted to JGR.

Dong, C., McWilliams, J.C., Shchepetkin, A.F., 2006. Island wakes in deep water. Journal of Physical Oceanography, in press.

Drake, D.E., Cacchione, D.A., 1985. Seasonal variation in sediment transport on the Russian River shelf. California. Continental Shelf Research 4 (5), 495–514.

Drake, D.E., Cacchione, D.A., 1989. Estimates of the suspended sediment reference concentration (c_a) and resuspension coefficient (γ_0) from near-bed observations on the California shelf. Continental Shelf Research 9, 51–64.

Drake, D.E., Cacchione, D.A., Karl, H.A., 1985. Bottom currents and sediment transport on San Pedro Shelf, California. Journal of Sedimentary Petrology 55 (1), 15–28.

Edwards, B.D., Dartnell, P., Chezar, H., 2003. Characterizing benthic substrates of Santa Monica Bay with seafloor photography and multibean sonar imagery. Marine Environmental Research 56, 47–66.

Egbert, G.D., Erofeeva, S.Y., 2002. Efficient inverse modeling of barotropic ocean tides. Journal of Atmospheric and Oceanic Technology 19 (2).

Emery, K.O., 1960. The Sea off Southern California: A Modern Habitat of Petroleum. Wiley, New York.

Garcia, M., Parker, G., 1991. Entrainment of bed sediment into suspension. Journal of Hydraulic Engineering 117 (4), 414–435.

Garrett, A.E., Holloway, G., 1984. Dissipation and diffusion by internal wave breaking. Journal of Marine Research 42, 15–27.

Gorsline, D.S., Grant, D.J., 1972. Sediment textural patterns on San Pedro Shelf, California (1951–1971): reworking and transport by waves and currents. In: Swift, D.J.P., Duane, D.B., Pilkey, O.H. (Eds.), Shelf Sediment Transport: Process and Pattern. Hutchinson and Ross Inc., Dowden, pp. 575–600.

Gorsline, D.S., Kolpack, R.L., Karl, H.A., Drake, D.E., Fleischer, P., Thronton, S.E., Schwalbach, J.R., Savrda, C.E., 1984. Studies of fine-grained sediment transport processes and products in the California Continental Borderland. In: Stow, D.A.V., Piper, D.J.W. (Eds.), Fine-grained Sediments: Deep-water Processes and Facies. Blackwell Science, Oxford, pp. 395–415.

Grant, W.D., Madsen, O.S., 1979. Combined wave and current interaction with a rough bottom. Journal of Geophysical Research 84, 1797–1808.

Grant, W.D., Madsen, O.S., 1982. Movable bed roughness in unsteady oscillatory flow. Journal of Geophysical Research 87, 469–481.

Harris, C.K., Wiberg, P.L., 2001. A two-dimensional, time-dependent model of suspended sediment transport and bed reworking for continental shelves. Computers and Geosciences 27, 675–690.

Harris, C.K., Wiberg, P.L., 2002. Across-shelf sediment transport: interactions between suspended sediment and bed sediment. Journal of Geophysical Research 107 (C1).

Hickey, B.M., 1992. Circulation over the Santa Monica–San Pedro Basin and Shelf. Progress in Oceanography 30, 37–115.

Hickey, B.M., Dobbins, E.L., Allen, S.E., 2003. Local and remote forcing of currents and temperature in the central Southern California Bight. Journal of Geophysical Research 108 (C3).

Large, W.G., Pond, S., 1981. Open ocean momentum flux measurements in moderate to strong winds. Journal of Physical Oceanography 11, 324–336.

Large, W.G., McWilliams, J.C., Doney, S.C., 1994. Oceanic vertical mixing: a review and a model with a nonlocal boundary layer parameterization. Reviews of Geophysics 32 (4), 363–404.

Lesser, G.R., Roelvink, J.A., van Kester, J.A.T.M., Stelling, G.S., 2004. Development and validation of a three-dimensional morphological model. Coastal Engineering 51 (8–9), 883–915.

Levitus, S., Boyer, T.P., 1994. World ocean Atlas 1994. NOAA Atlas NESDIS 3, vol. 4: Temperature, NODC. Silver Spring, MD, 129pp.

Levitus, S., Burgett, R., Boyer, T.P., 1994. World ocean Atlas 1994. NOAA Atlas NESDIS 3, vol. 3: Salinity, NODC. Silver Spring, MD, 111pp.

Li, M.Z., Amos, C.L., 2001. Sedtrans96: the upgraded and better calibrated sediment-transport model for continental shelves. Computers and Geosciences 27, 619–645.

Liu, X.D., Osher, S., Chan, T., 1994. Weighted essentially non-oscillatory schemes. Journal of Computational Physics 115, 200–212.

Luyten, P.J., Jones, J.E., Proctor, R., Tabor, A., Tett, P., Wild-Allen, K., 1999. COHERENS. A coupled hydrodynamical-ecological model for regional and shelf seas: user documentation. MUMM Report, Management Unit of the Mathematical Models of the North Sea, Brussels, 914pp.

Marchesiello, P., McWilliams, J.C., Shchepetkin, A.F., 2001. Open boundary conditions for long-term integration of regional oceanic models. Ocean Modelling 3, 1–20.

Marchesiello, P., McWilliams, J.C., Shchepetkin, A.F., 2003. Equilibrium structure and dynamics of the California current system. Journal of Physical Oceanography 33 (4), 753–783.

McWilliams, J.C., Restrepo, J.M., Lane, E.M., 2004. An asymptotic theory for the interaction of waves and currents in shallow coastal waters. Journal of Fluid Mechanics 511, 135–178.

Nezlin, N.P., DiGiacomo, P.M., 2005. Satellite ocean color observations of stormwater runoff plumes along the San Pedro Shelf (southern California) during 1997–2003. Continental Shelf Research 25 (14), 1692–1711.

Niedoroda, A.W., Swift, D.J.P., Reed, C.W., Stull, J.K., 1996. Contaminant dispersal on the Palos Verdes continental margin: III. Processes controlling transport, accumulation and re-emergence of DDT-contaminated sediment particles. Science of the Total Environment 179, 109–133.

Noble, M.A., Xu, J.P., 2003. Observations of large-amplitude cross-shore internal bores near the shelf break, Santa Monica Bay, CA. Marine Environmental Research 56, 127–149.

O'Reilly, W.C., Guza, R.T., 1993. A comparison of two spectral wave models in the Southern Californian Bight. Coastal Engineering 19, 263–282.

Penven, P., Debreu, L., Marchesiello, P., McWilliams, J.C., 2006. Evaluation and application of the 1-way embedding procedure to the California Current Upwelling System. Ocean Modelling 12, 157–187.

Reed, C.W., Niederoda, A.W., Swift, D.J.P., 1999. Modeling sediment entrainment and transport processes limited by bed armoring. Marine Geology 154, 143–154.

Shchepetkin, A.F., McWilliams, J.C., 1998. Quasi-monotone advection schemes based on explicit locally adaptive dissipation. Monthly Weather Review 126, 1541–1580.

Shchepetkin, A.F., McWilliams, J.C., 2003. A method for computing horizontal pressure gradient force in an ocean model with a non-aligned vertical coordinate. Journal of Geophysical Research 108 (C3).

Shchepetkin, A.F., McWilliams, J.C., 2005. The regional oceanic modeling system (ROMS): a split-explicit, free-surface, topography-following-coordinate oceanic model. Ocean Modelling 9 (4), 347–404.

Sherwood, C.R., Drake, D.E., Wiberg, P.L., Wheatcroft, R.A., 2002. Prediction of the fate of p, p′-DDE in sediment on the Palos Verdes shelf California, USA. Continental Shelf Research 22 (6–7), 1025–1058.

Smith, J.D., 1977. Modeling sediment transport on continental shelves. In: Goldberg, E.D., McCave, I.N., O'Brien, J.J., Steele, J.H. (Eds.), The Sea. Wiley-Interscience, New York, pp. 539–577.

Smith, J.D., McLean, S.R., 1977. Spatially averaged flow over a wavy bed. Journal of Geophysical Research 82, 1735–1746.

Smith, W.H.F., Sandwell, D.T., 1997. Global seafloor topography from satellite altimetry and ship depth soundings. Science 277 (5334), 1956–1962.

Sommerfield, C.K., Lee, H.J., 2003. Magnitude and variability of Holocene sediment accumulation in Santa Monica Bay, California. Marine Environmental Research 56, 151–176.

Soulsby, R.L., 1995. Bed shear-stresses due to combined waves and currents. In: Stive, M.J.F., et al. (Eds.), Advances in Coastal Morphodynamics, Wiley, pp. 4.20–4.23.

Soulsby, R.L., 1997. Dynamics of Marine Sands. Telford Publ., London.

Soulsby, R.L., Whitehouse, R.J.S.W., 1997. Threshold of sediment motion in coastal environments. In: Stive, M.J.F., et al. (Eds.), Proceedings of the Pacific Coasts and Ports'97 Conference. University of Canterbury, New Zealand, Christchurch, pp. 149–15423.

Styles, R., Glenn, S.M., 2000. Modeling stratified wave and current bottom boundary layers on the continental shelf. Journal of Geophysical Research 105(C10), 24,119–24,139.

Walgreen, M., De Swart, H.E., Calvete, D., 2003. Effect of grain size sorting on the formation of shoreface-connected sand ridges. Journal of Geophysical Research 108 (C3).

Wang, X., Chao, Y., Li, Z., Dong, C., Farrara, J., McWilliams, J.C., Shum, C.K., Wang, Y., Matsumoto, K., Rosenfeld, L.K., Paduan, J.D., 2006. Tidal simulation using regional ocean modeling systems (ROMS). Presented at 15 Years of Progress in Radar Altimetry, Venice, Italy, March 13–18, 2006. JPL, Pasadena, CA.

Warner, J.C., Sherwood, C.R., Arango, H.G., Signell, R.P., 2005. Performance of four turbulence closure models implemented using a generic length scale method. Ocean Modelling 8, 81–113.

Wiberg, P.L., Harris, C.K., 2002. Desorption of p, p′-dde from sediment during resuspension events on the Palos Verdes shelf, California: a model approach. Continental Shelf Research 22 (6–7), 1005–1023.

Wiberg, P.L., Drake, D.E., Cacchione, D.A., 1994. Sediment resuspension and bed armoring during high bottom stress events on the northern California inner continental shelf: measurements and predictions. Continental Shelf Research. 14 (10/11), 1191–1219.

Wiberg, P.L., Drake, D.E., Harris, C.K., Noble, M., 2002. Sediment transport on the Palos Verdes shelf over seasonal to decadal time scales. Continental Shelf Research 22, 987–1004.

Xu, J.P., 2005. Observations of plan-view sandripple behavior and spectral wave climate on the inner shelf of San Pedro Bay, California. Continental Shelf Research 25, 373–396.

Xu, J.P., Noble, M., Eittreim, S.L., 2002. Suspended sediment transport on the continental shelf near Davenport, California. Marine Geology 181, 171–193.

Yalin, M.S., 1964. Geometrical properties of sand waves. Journal of Hydraulic Division, Proceedings of ASCE 90 (HY5), 105–119.

Zhang, Y., Swift, D.J.P., Fan, S., Niedoroda, A.W., Reed, C.W., 1999. Two-dimensional numerical modeling of storm deposition on the northern California shelf. Marine Geology 154, 155–167.